Journal of Materials Chemistry C

RSC Publishing

PAPER

View Article Online
View Journal | View Issue

Synthesis, optical properties and charge transport characteristics of a series of novel thiophene-fused phenazine derivatives†

Cite this: *J. Mater. Chem. C*, 2013, **1**, 3467

Yongfa Xie,[a] Takuya Fujimoto,[a] Simon Dalgleish,[a] Yoshiaki Shuku,[a] Michio M. Matsushita*[a] and Kunio Awaga*[ab]

A series of tetrathienophenazine derivatives (***t*-TTP**, ***l*-TTP**, ***m*-TTP** and their alkyl-substituted derivatives) have been synthesized *via* a simple condensation reaction between diketones and diamines. The redox potentials, UV-vis absorption spectra and fluorescence spectra of these derivatives are significantly affected by the positions of the sulfur atoms and the alkyl groups. The observed electronic properties were well reproduced by theoretical calculations based on density functional theory. X-ray analyses of these derivatives reveal extensive π–π interactions and short S···S contacts. The alkyl-substituted derivatives afford highly crystalline thin films by vapor deposition, and show reasonable field effect transistor performance. The conductivity of doped single crystals of these materials was also investigated, and showed an increase by several orders of magnitude upon I_2 vapor doping. The π–π stacked structures of these crystals and conductive properties indicate that these thiophene-fused phenazines are useful materials for application in organic electronics.

Received 22nd February 2013
Accepted 28th March 2013

DOI: 10.1039/c3tc30346b

www.rsc.org/MaterialsC

Introduction

Organic π-conjugated materials have attracted considerable attention in recent years due to their potential application in organic electronics such as organic light emitting diodes (OLEDs),[1] organic photovoltaics (OPVs)[2] and organic field transistors (OFETs).[3] Within this field, thiophene-fused polyaromatic compounds have received sustained interest since the thienyl S···S contacts can contribute to the intermolecular charge transport in the solid state, as well as affect the π–π stacking behavior. Some thiophene-fused polyaromatic compounds have shown high-performance in OFET devices, with figures of merit rivaling that of amorphous silicon. Diacene-fused thieno[3,2-*b*]-thiophenes (up to 12 cm^2 V^{-1} s^{-1} of field-effect mobility),[4] 2,6-diaryl-NDTs (up to 0.1 cm^2 V^{-1} s^{-1} of field-effect mobility)[5] and 2,7-dialkyl[1]-benzothieno[3,2-*b*][1]benzothiophenes (C_n-BTBTs) (up to 2.7 cm^2 V^{-1} s^{-1} of field-effect mobility)[6] are some representative examples.

However, the preparation of such molecules usually involves many steps, and utilizes toxic organometallic chemicals. In the present work, we have designed and synthesized a series of thiophene-fused phenazines (***t*-TTP**, ***l*-TTP** and ***m*-TTP**) and their alkyl-substituted derivatives (Scheme 1). All of these derivatives were obtained by a key reaction, a condensation reaction between a diketone and a diamine, itself derived from the diketone.[7] Crystals of these derivatives were obtained by recrystallization in solution or by sublimation, and all of the derivatives afforded crystalline thin films by vapor deposition. The physical properties, crystal structures and transport properties of these molecules were compared with each other in terms of the positions of sulfur atoms, and the effect of the nitrogen atoms in the central aromatic ring is discussed in comparison with the anthracene analogues reported by Perepichka[8] and Pei[9] (Scheme 1).

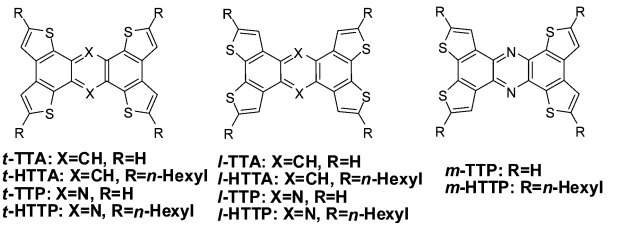

Scheme 1 Chemical structure of phenazine derivatives (X = N) and anthracene analogues (X = CH).

[a]*Department of Chemistry & Research Center for Materials Science, Nagoya University, Furo-cho, Chikusa-ku, Nagoya 464-8602, Japan. E-mail: mmmatsushita@nagoya-u.jp; Awaga@mbox.chem.nagoya-u.ac.jp*

[b]*CREST, JST, Furo-cho, Chikusa-ku, Nagoya 464-8602, Japan*

† Electronic supplementary information (ESI) available: Cyclic voltammetry, thin-film XRD, and theoretical calculations. CCDC 924738 and 924748–924750. For ESI and crystallographic data in CIF or other electronic format see DOI: 10.1039/c3tc30346b

Results

Synthesis

The synthetic route to the tetrathienophenazines (***t*-TTP**, ***l*-TTP**, ***m*-TTP**, ***t*-HTTP**, ***l*-HTTP** and ***m*-HTTP**) is outlined in Scheme 2. The phenazine skeleton was formed by a condensation reaction between a diketone and a diamine.[10] For example, ***t*-TTP** was obtained in 79% yield by refluxing the diketone **1a** and the diamine **4a** in ethanol. Diamine **4a** was prepared in 67% yield from dioxime **3a** by reduction with stannous chloride, and dioxime **3a** can be obtained from **1a** by reaction with hydroxylamine hydrochloride in nearly quantitative yield. Diketones **1a** and **2a** were prepared in accordance with the literature.[11] Hexylated diketones **1b** and **2b** were synthesized from hexyl thiophene, as shown in Scheme 3. The unsubstituted derivatives (***t*-TTP**, ***l*-TTP** and ***m*-TTP**) showed poor solubility in common organic solvents such as toluene, dichloromethane and chloroform, while the solubility was much improved by substituting the hexyl groups at the α-position of the fused thiophene rings (***t*-HTTP**, ***l*-HTTP** and ***m*-HTTP**).

Electrochemical properties

The electrochemical properties of these derivatives were characterized by cyclic voltammetry (CV). The unsubstituted derivatives did not show any redox peaks within the electrochemical window of tetrabutylammonium hexafluorophosphate ($(n\text{-}Bu_4N)PF_6$) in dichloromethane (DCM) solution. On the other hand, thin films of these molecules deposited on an ITO electrode showed gradually increasing redox waves upon cycling

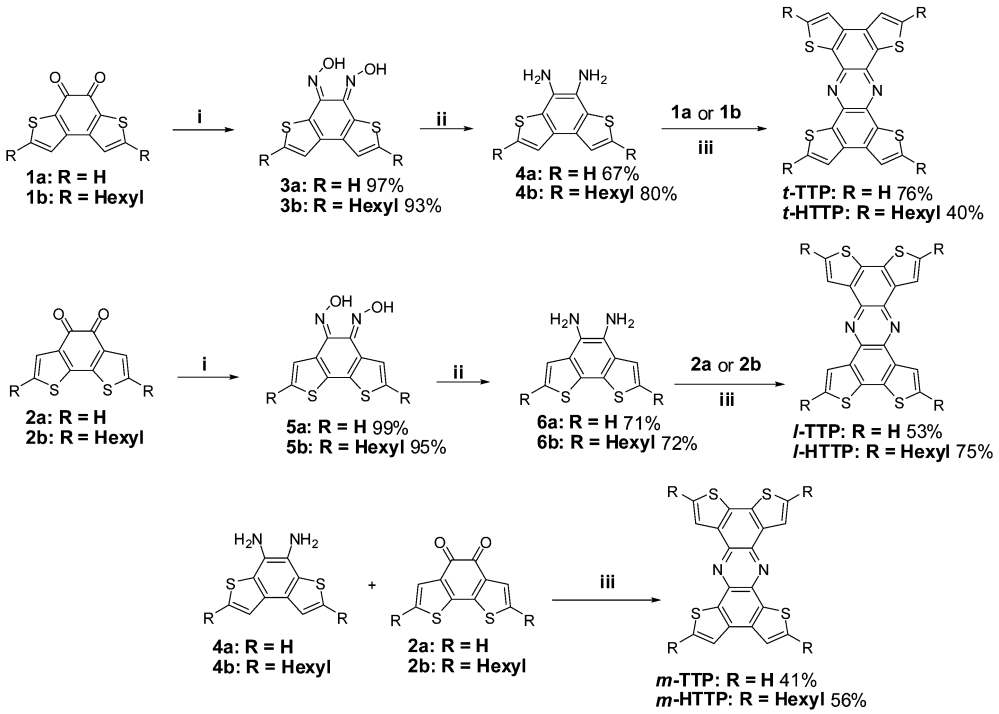

Reagents and conditions: (i) $NH_2OH{\cdot}HCl$, Pyridine/EtOH, 90 °C; (ii) $SnCl_2$, HCl(con.), EtOH, 0 °C ~ RT; (iii) EtOH, reflux.

Scheme 2 Synthesis of thiophene-fused phenazines. *Reagents and conditions*: (i) $NH_2OH{\cdot}HCl$, pyridine/EtOH, 90 °C; (ii) $SnCl_2$, HCl (con.), EtOH, 0 °C to RT; (iii) EtOH, reflux.

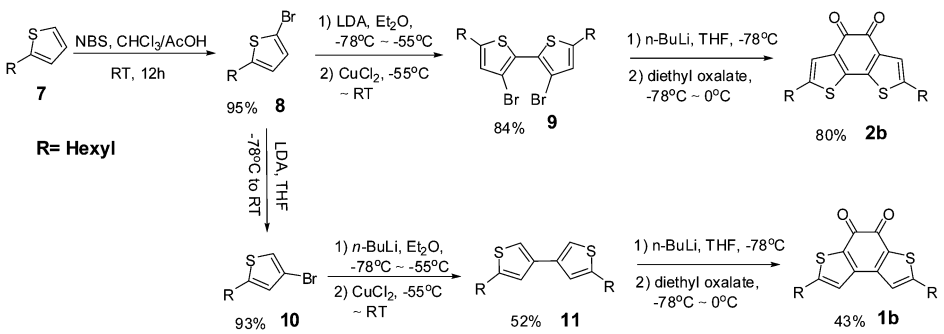

Scheme 3 Synthesis of diketone compounds.

(Fig. S1†). This behavior resembles the redox properties of the corresponding anthracene analogues, and can be explained by the formation of small amounts of the radical cation species, which is followed by the polymerization at the α-position.[8] However, the alkyl-substituted derivatives showed reproducible cyclic voltammograms with two oxidation peaks, although the corresponding reduction peaks were not observed (Fig. 1). From these redox potentials (1.06 V, 0.83 V and 1.21 V *vs.* Fc/Fc^+ for ***l*-HTTP**, ***m*-HTTP** and ***t*-HTTP**, respectively), the HOMO levels of these molecules were estimated to be −6.2 eV, −5.9 eV and −6.3 eV for ***l*-HTTP**, ***m*-HTTP** and ***t*-HTTP**, respectively.[12] These values indicate that these phenazine derivatives are weaker donors in comparison with the corresponding tetrathienoanthracene analogue 8 (−5.9 eV and −6.0 eV for ***l*-HTTA** and ***t*-HTTA**, respectively).

Optical properties

The UV-vis absorption spectra of the tetrathienophenazine derivatives in $CHCl_3$ are shown in Fig. 2, and their λ_{max} are summarized in Table 1. In all cases, two strong absorption bands are observed; one absorption band lies around 310 nm for all derivatives, while the other absorption band lies between 400 nm and 490 nm, depending on the structure. Introduction of alkyl chains at the α-positions of the fused thiophenes results in a bathochromic shift (3–20 nm) of the λ_{max} values in comparison with their unsubstituted derivatives (Fig. 2). The λ_{max} of the unsubstituted derivatives follows the progression ***l*-TTP** > ***m*-TTP** > ***t*-TTP**, and this tendency of absorption bands was also maintained in the corresponding alkyl-substituted derivatives (Fig. 2). These features in the absorption spectra were well reproduced by time-dependent Density Functional Theory (TD-DFT) calculations, as discussed later.[13]

The three unsubstituted derivatives (***l*-TTP**, ***m*-TTP** and ***t*-TTP**) showed light-blue fluorescence (λ^{fl}_{max}: around 480 nm) in chloroform while ***t*-HTTP** showed green fluorescence (λ^{fl}_{max}: 501 nm), and both ***m*-HTTP** and ***l*-HTTP** showed yellow fluorescence (λ^{fl}_{max}: around 530 nm). Fig. 3 shows the fluorescence spectra of these derivatives, and the maximum emissions are listed in Table 1. Introduction of the alkyl-chains also caused a red shift in the fluorescence peaks. The Stokes shift of each material is 0.46 eV, 0.25 eV and 0.07 eV for ***l*-TTP**, ***m*-TTP**, and ***t*-TTP**, respectively, and a decrease in the Stokes shifts was also observed in the alkyl-substituted derivatives (Table 1). The fluorescence absolute quantum yields (Φ_f) of these materials were in the range of 0.02–0.19, as listed in Table 1.

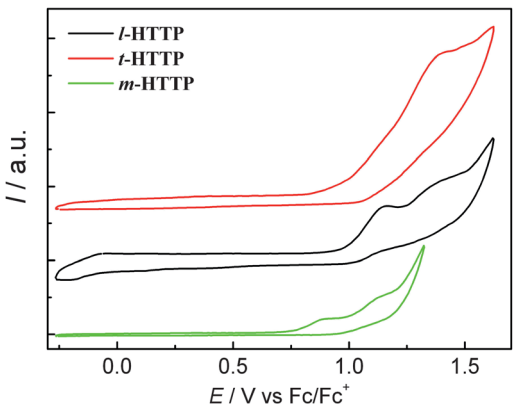

Fig. 1 Cyclic voltammograms (scan rate 100 mV s^{-1}) of ***l*-HTTP**, ***t*-HTTP** and ***m*-HTTP** recorded in DCM solution containing (n-Bu_4N)PF_6 (0.1 M) as an electrolyte. A glassy carbon electrode and a Pt electrode were used as the working electrode and the counter electrode, respectively. Potentials were referenced to Fc/Fc^+.

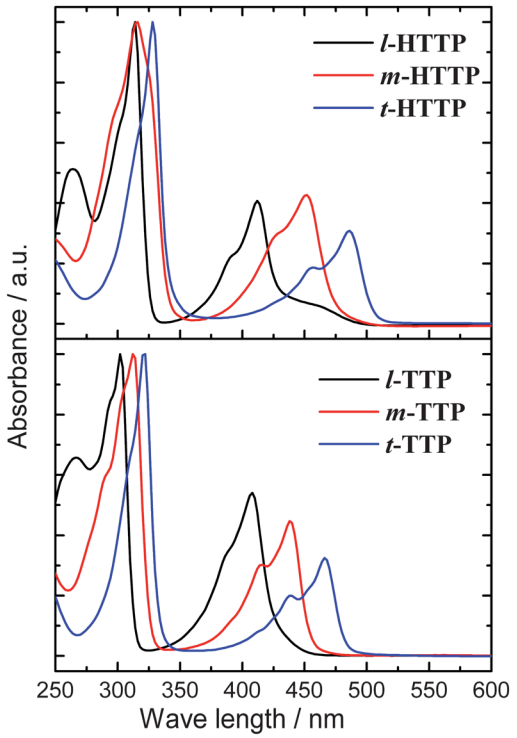

Fig. 2 Comparison of the UV-vis spectra of thiophene-fused phenazines in $CHCl_3$ solution.

X-ray crystallography

From the six newly prepared derivatives, four derivatives (***t*-TTP**, ***m*-TTP**, ***l*-TTP** and ***l*-HTTP**) could be crystallized by solution or sublimation methods to afford single crystals suitable for X-ray diffraction. The cell parameters of these crystals are listed in Table 2. All of the unsubstituted derivatives (***t*-TTP**, ***m*-TTP** and ***l*-TTP**) have different space groups and cell parameters depending on the different positions of sulfur atoms in the skeleton. ***t*-TTP** (Fig. 4) showed nearly the same cell parameter and packing structure as its corresponding anthracene analogue (***t*-TTA**), although the shortest S···S contacts and π–π intermolecular distances (3.664(1) Å and 3.43 Å) are different from those of ***t*-TTA** (3.769(1) Å and 3.354(3) Å). ***l*-TTP** showed a different crystal structure from that of the corresponding anthracene analogue (***l*-TTA**).[8] The ***l*-TTP** crystal consists of two columns of slipped π-stacked (along the *b* axis) molecules with a π–π intermolecular distance of 3.48 Å (Fig. 5). The ***l*-HTTP** crystal consists of slipped π-stacked molecules along the *a* axis with a shorter π–π intermolecular

Table 1 Electrochemical[a] and optical properties of thiophene-fused phenazines, compared to theoretical values

	l-TTP	*m*-TTP	*t*-TTP	*l*-HTTP	*m*-HTTP	*t*-HTTP	*l*-TTA[f]	*t*-TTA[f]
$E_{1/2}^{exp\,a}$ (V)	—	—	—	1.06	0.83	1.21	—	—
$E_{HOMO}^{exp\,b}$ (eV)	—	—	—	−6.21	−5.93	−6.33	−6.22	−6.69
$E_{HOMO}^{calcd\,c}$ (eV)	−5.60	−5.64	−5.68	−5.19	−5.21	−5.32	−5.18	−5.23
$E_{LUMO}^{calcd\,c}$ (eV)	−2.27	−2.33	−2.39	−2.04	−1.92	−2.11	—	—
E_g^{calcdc} (eV)	3.33	3.31	3.29	3.15	3.29	3.21	3.52	3.50
$\lambda_{max}^{abs\,d}$ (nm)	408	439	467	411	451	486	379	418
$\lambda_{max}^{abs\,d}$ (nm)	375	404	432	379	414	444	—	—
$\lambda_{max}^{fl\,d}$ (nm)	480	481	479	526	534	501	398	422
Φ_f^e	0.02	0.02	0.19	0.15	0.05	0.18	0.17	0.32
Stokes shift[d] (eV)	0.46	0.25	0.07	0.66	0.43	0.07	0.16	0.03

[a] Measured in DCM, (n-Bu_4N)PF_6 (0.1 M) as the supporting electrolyte and referenced to Fc/Fc^+. [b] Estimated from the CV measurement according to the empirical formula $E_{HOMO} = -(1.4 \pm 0.1) \times qV_{CV} - (4.6 \pm 0.08)$ eV from ref. 12. [c] B3LYP/6-31G(d). [d] Measured in $CHCl_3$. [e] Absolute fluorescence quantum yields were determined with a Hamamatsu C9920-02 calibrated integrating sphere system. [f] Cited from ref. 8.

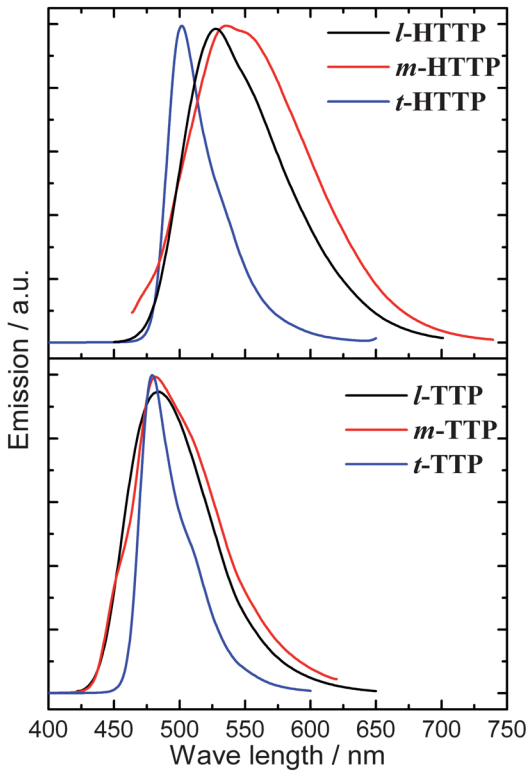

Fig. 3 Photoluminescence spectra of thiophene-fused phenazines in $CHCl_3$ solution (λ_{ex} 322 nm for ***t*-TTP**, 316 nm for ***m*-TTP**, 303 nm for ***l*-TTP**, 370 nm for ***l*-HTTP**, 380 nm for ***t*-HTTP**, and 380 nm for ***m*-HTTP**).

distance (3.40 Å) than that of ***l*-TTP** (3.48 Å) (Fig. 6). The crystal of ***m*-TTP** also showed a slipped π-stacking structure with a π–π intermolecular distance of 3.46 Å. Since the dipole moments of molecular stacks do not completely compensate each other in the crystal cell, ***m*-TTP** is a polar crystal (Fig. 7).

Preparation, characterization, and FET performance of thin-films

Thin films of the alkyl-substituted tetrathienophenazine derivatives were prepared by vapor deposition on Si substrates (with SiO_2 on the surface). X-ray diffraction analyses of the thin films yielded information on the molecular arrangements in the films. Thin-film X-ray diffraction of ***l*-HTTP** grown under different conditions shows sharply resolved peaks assignable to multiple reflections, indicating crystalline order in the direction of the substrate normal (Fig. 8). Thin films deposited on the untreated and HMDS (hexamethyldisilazane) treated Si substrates at T_{sub} = 25 °C consisted of two series of multiple (00l) and (00l') reflections, while thin films deposited at T_{sub} = 75 °C showed only one series of multiple (00l) reflections. However, neither the (00l) nor (00l') peaks were assignable to the simulated powder pattern of the single-crystal phase of ***l*-HTTP**. These results suggest that the vapor-deposited thin films of ***l*-HTTP** have distinct phases from the single crystalline phase. The interlayer spacing (d), determined from the first-layer line of the XRD pattern, are 19.4 Å and 24.3 Å for the (00l) and (00l') reflections, respectively. This result suggests that the thin film contains only one molecular arrangement on the substrate when deposited at higher temperature. In addition, the thin films deposited at T_{sub} = 75 °C showed larger grains (width: 0.25–0.5 μm and height: 10.0–30.0 nm), and tighter packing on the substrates than thin films deposited at room temperature (width: 0.5–1.5 μm and height: 20.0–40.0 nm) as observed from AFM images (Fig. 9).

Table 2 Crystal data and intermolecular contacts

	t-TTP	*l*-TTP	*m*-TTP	*l*-HTTP
Space group	$P2_1/n$	$P2_1/a$	$P2_1$	$P\bar{1}$
a (Å)	11.247(5)	17.064(2)	12.581(1)	4.894(1)
b (Å)	5.014(2)	3.894(4)	4.8247(5)	12.751(3)
c (Å)	14.169(6)	25.72(3)	13.718(1)	17.057(5)
α (deg)	—	—	—	76.147(1)
β (deg)	91.668(7)	108.820(2)	96.563(2)	84.810(1)
γ (deg)	—	—	—	72.178(1)
R, R_w	0.0618, 0.1027	0.1284, 0.2638	0.0502, 0.1370	0.0627, 0.0718
S···S[a] (Å)	3.664(1)	3.686(2)	4.073(1)	—
δ^b (Å)	3.43	3.48	3.46	3.40

[a] The shortest S···S′ contacts. [b] δ is the averaged inter-planar distance between molecules along the π-stack.

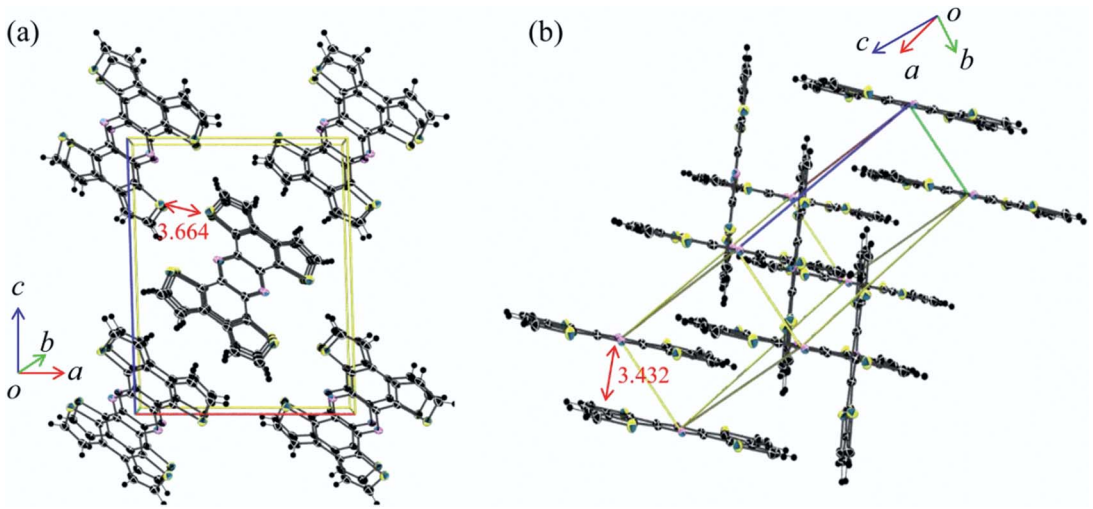

Fig. 4 (a) Crystal structure of ***t*-TTP**. S···S′ contacts. (b) π···π distance between the molecules (unit: Å).

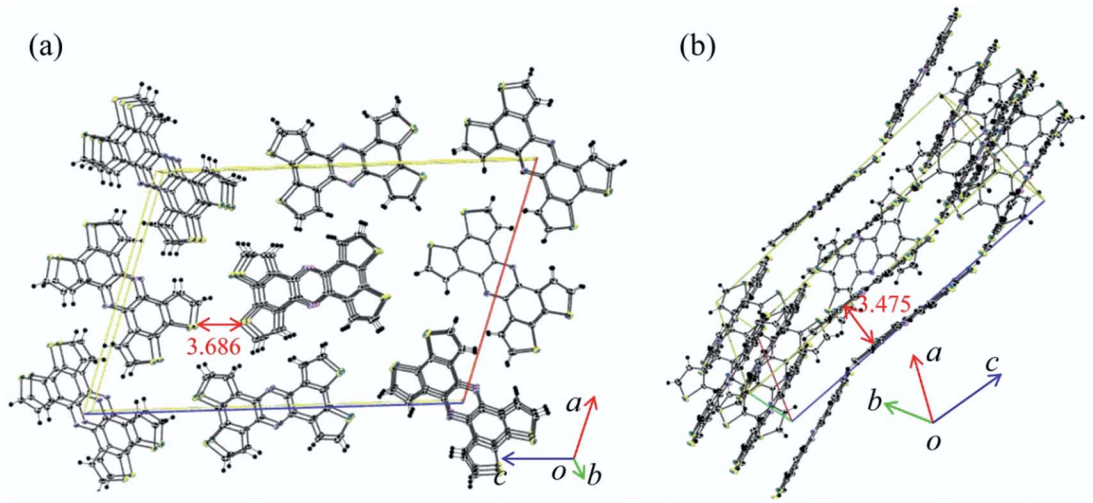

Fig. 5 (a) Crystal structure of ***l*-TTP**. (b) S···S′ contacts. The π···π distance between the molecules (unit: Å).

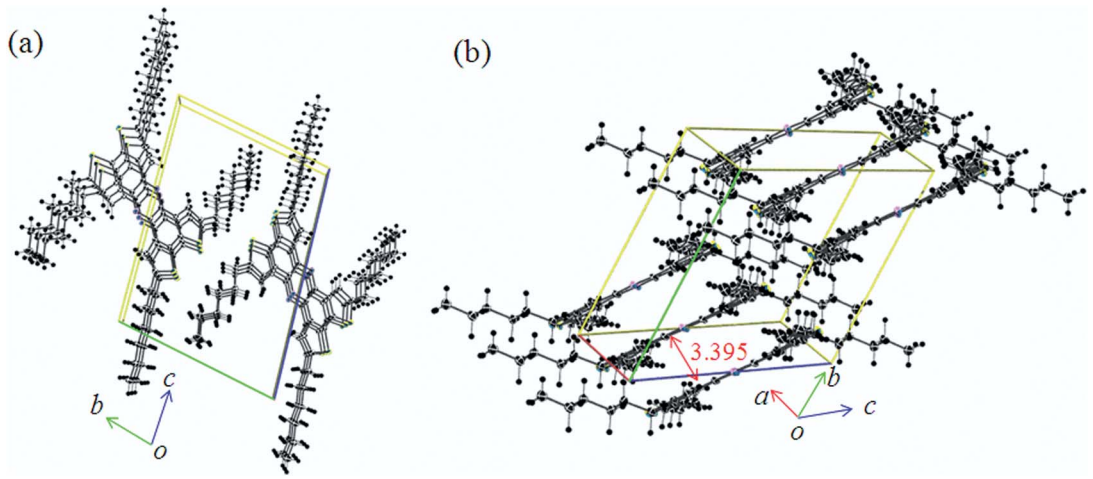

Fig. 6 Crystal structure of ***l*-HTTP**. (a) View along the *a* axis. (b) π···π distance between the molecules (unit: Å).

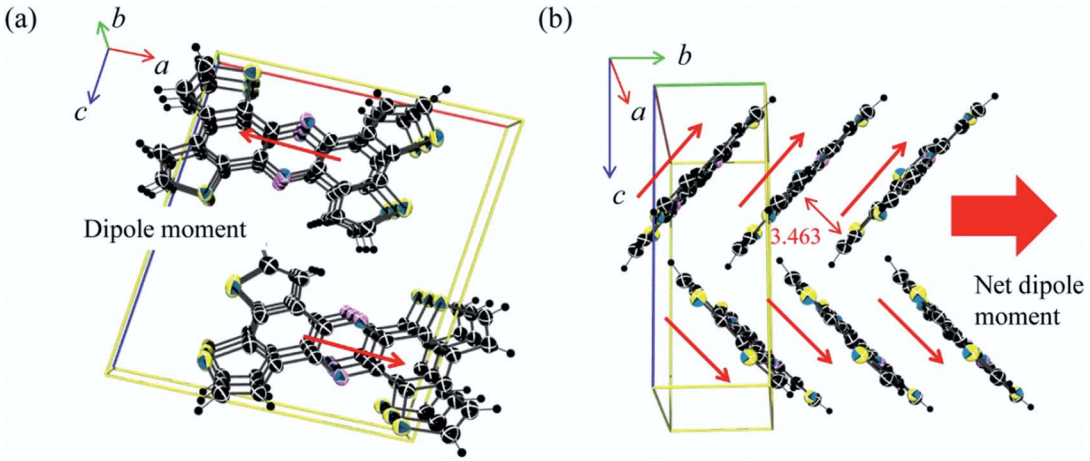

Fig. 7 Crystal structure of ***m*-TTP**. (a) Dipole moment of the molecular stacks. (b) $\pi\cdots\pi$ distance between the molecules and direction of the dipole moment (unit: Å).

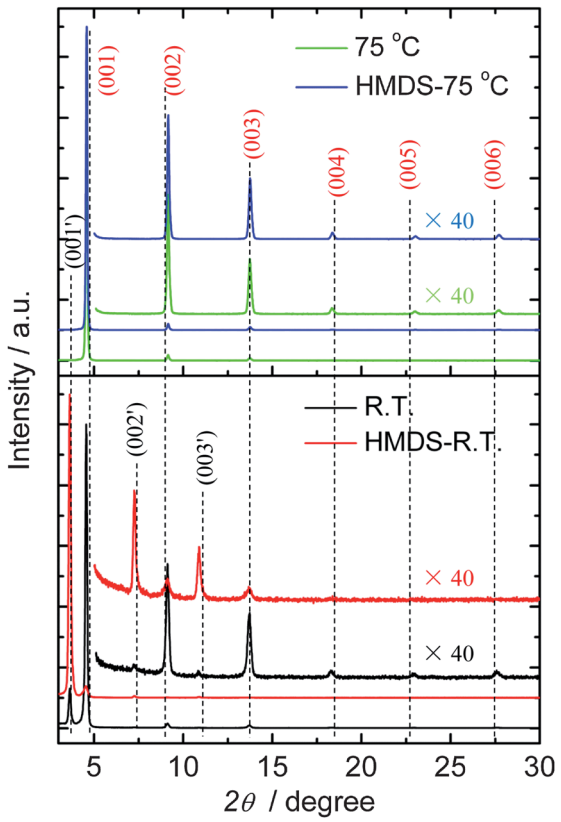

Fig. 8 Out-of-plane XRD pattern of ***l*-HTTP** thin films (50 nm) at different substrate temperatures (no in-plane signal).

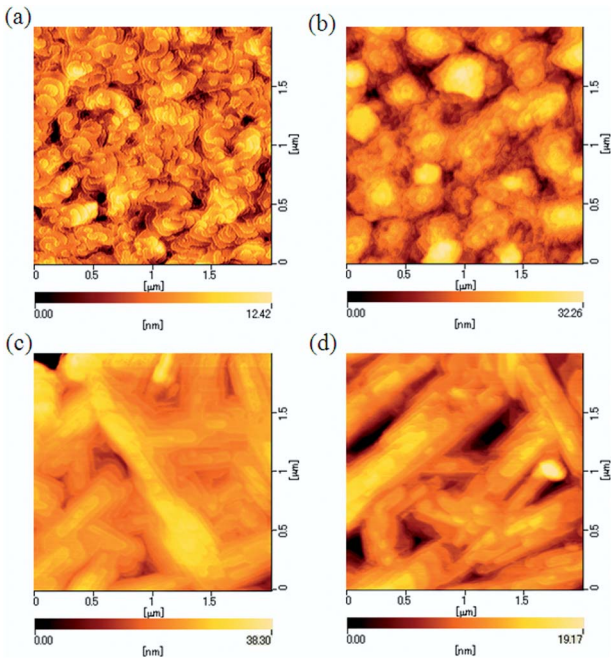

Fig. 9 AFM images of thin films of ***l*-HTTP** on bare substrates with T_{sub} = 25 °C (a), substrates treated with HMDS with T_{sub} = 25 °C (b), bare substrates with T_{sub} = 75 °C (c) and substrates treated with HMDS with T_{sub} = 75 °C (d).

Organic field-effect transistor (OFET) devices of these derivatives were prepared on bottom-gate, bottom-contact substrates by vacuum deposition. The thin films of ***l*-HTTP** deposited at room temperature on surface-oxidized silicon substrates showed FET characteristics. The field-effect mobilities for this compound were $\mu_h = 1.2 \times 10^{-8}$ cm^2 V^{-1} s^{-1} and $\mu_h = 4.6 \times 10^{-9}$ cm^2 V^{-1} s^{-1} for untreated and HMDS treated substrates (Table 3), respectively. These values were greatly improved by increasing the substrate temperature during vapor deposition: $\mu_h = 6.2 \times 10^{-6}$ cm^2 V^{-1} s^{-1} and $\mu_h = 3.2 \times 10^{-6}$ cm^2 V^{-1} s^{-1} for untreated and treated substrates (T_{sub} = 75 °C), respectively. The on/off ratio and threshold voltage of the FET devices are listed in Table 3. These results suggest that the mono-oriented phase and bigger grains in the thin films can improve the transistor performance, while the HMDS treatment on the SiO_2 surface does not yield an obvious effect on the ***l*-HTTP** thin film transistor characteristics.

Thin films of ***m*-HTTP** and ***t*-HTTP** were also prepared by vapor deposition at T_{sub} = 75 °C on the Si substrates without HDMS treatment. The thin films of these materials also showed high crystallinity, characterized by thin-film XRD (Fig. S2†). These films also showed FET characteristics with field-effect

Table 3 Thin film properties of thiophene-fused phenazines

	Surface treatment	T_{sub}[a]	*d*-Spacing/Å	μ_h/cm^2 V^{-1} s^{-1}	$I_{on/off}$	V_{th}/V
***l*-HTTP**	HMDS	25 °C	24.3 19.4	1.2×10^{-8}	10^3	—
***l*-HTTP**	Bare	25 °C	24.3 19.4	4.6×10^{-9}	10^4	—
***l*-HTTP**	HMDS	75 °C	19.4	3.2×10^{-6}	10^4	−33
***l*-HTTP**	Bare	75 °C	19.4	6.2×10^{-6}	10^4	−24
***t*-HTTP**	Bare	75 °C	19.0	2.9×10^{-6}	10^5	−23
***m*-HTTP**	Bare	75 °C	20.2	2.5×10^{-6}	10^4	−38

[a] Substrate temperature upon vapor deposition.

mobilities of $\mu_h = 2.9 \times 10^{-6}$ cm^2 V^{-1} s^{-1} and $\mu_h = 2.5 \times 10^{-6}$ cm^2 V^{-1} s^{-1} for ***t*-HTTP** and ***m*-HTTP**, respectively (Fig. S4† and Table 3). The substitution dependence of the tetrathienophenazines on the FET characteristics is similar to that of the anthracene analogues: the alkyl-substituted anthracene analogues showed reasonable transistor performance (∼10^{-2} cm^2 V^{-1} s^{-1}), while the unsubstituted anthracene analogues did not show a field effect.[8]

Chemical doping effect on transport properties

Since all of the thiophene-fused phenazine derivatives afforded crystalline thin films by vapor deposition (for thin-film XRD characterization of unsubstituted derivatives, see Fig. S3†), the conductivities of these thin films were studied as well. In all cases, the conductivities were improved by several orders of magnitude upon I_2 doping (Fig. S5† and Table 4). The single crystals of these (four) derivatives also showed an increase in conductivity upon I_2 doping. The change in conductivities of the iodine-doped single crystals (10^{-7} to 10^{-5} Ω^{-1} cm^{-1} to 10^{-2} to 10^{-1} Ω^{-1} cm^{-1}) was much higher than those of the thin films (10^{-11} to 10^{-8} Ω^{-1} cm^{-1} to 10^{-7} to 10^{-5} Ω^{-1} cm^{-1}). This is reasonable because the continuous molecular π-stacking structure in the single crystals should be better suited for charge transport than that in the thin films with many grain boundaries.

Theoretical calculations

The molecular orbital calculations on the tetrathienophenazine derivatives and the corresponding anthracene analogues were carried out based on density functional theory. The energy levels of the HOMO and LUMO for each molecule are listed in Table 1, and the energy diagrams are shown in Fig. 10 accompanied by the spatial distributions of the molecular orbitals. The HOMO levels of the unsubstituted tetrathienophenazine derivatives were estimated to be −5.60, −5.64, and −5.68 eV for ***l*-TTP**, ***m*-TTP**, and ***t*-TTP**, respectively. These values are lower than those of typical thiophene-fused aromatic molecules such as the anthracene analogues (−5.18 to −5.23 eV)[8] and diacene-fused thieno[3,2-*b*]-thiophenes (−4.88 to −5.58 eV).[4a] This result is consistent with the experimental results from electrochemical measurements, and can be attributed to the introduction of an electron-deficient aromatic ring. The energy levels of LUMOs of the unsubstituted tetrathienophenazine derivatives were −2.27, −2.33, and −2.39 eV for ***l*-TTP**, ***m*-TTP**, and ***t*-TTP**, respectively. The ordering of the LUMO energy levels follows the same progression as those of the HOMOs, while the difference between the LUMO levels was slightly larger than that of the HOMOs. Therefore, the HOMO–LUMO gaps in these molecules are in the order ***l*-TTP** > ***m*-TTP** > ***t*-TTP**. This tendency was also observed in the optical band-gaps of these molecules, obtained experimentally, although the observed optical transitions are not due to transitions between the HOMO and LUMO, as discussed later.

Although the energetic orders are not usually the same for each molecule, all the molecules show the same sets of molecular orbitals because all the molecules are based on the same shape of the π-conjugating skeleton. The energy and the coefficients of the molecular orbitals of each atom are affected by the positions of sulfur atoms and the introduction of nitrogen atoms, compared to the anthracene analogues. For example, the LUMO of the unsubstituted derivatives have the same orbital symmetry as each other, while the orbital symmetry of the HOMOs was not the same, and varied depending on the positions of sulfur atoms (Fig. 10).

TD-DFT calculations were carried out to assign the optical transitions. The predicted absorption spectra of the thiophene-fused phenazines were in agreement with the experimental values, with an energy scaling factor of 0.94, as shown in Fig. S6–S11.† The transitions for the characteristic absorption bands are summarized in Table S1.† The TD-DFT calculations of the excited states of the unsubstituted derivatives also agreed with the fluorescence spectra (Fig. S14–S16†).

To evaluate the charge transport properties of the obtained crystals, the intermolecular hopping carrier mobility was calculated on the basis of Marcus theory.[14] The calculated

Table 4 Conductivity improvement of thiophene-fused phenazines doped by I_2 vapor in the crystal state and thin-film state (unit: Ω^{-1} cm^{-1})

	Crystal	Thin-film
***l*-TTP**	$10^{-5} \rightarrow 10^{-1}$	$10^{-10} \rightarrow 10^{-7}$
***m*-TTP**	$10^{-7} \rightarrow 10^{-2}$	$10^{-8} \rightarrow 10^{-5}$
***t*-TTP**	$10^{-7} \rightarrow 10^{-2}$	$10^{-9} \rightarrow 10^{-6}$
***l*-HTTP**	$10^{-6} \rightarrow 10^{-2}$	$10^{-9} \rightarrow 10^{-5}$
***m*-HTTP**	—	$10^{-11} \rightarrow 10^{-5}$
***t*-HTTP**	—	$10^{-11} \rightarrow 10^{-5}$

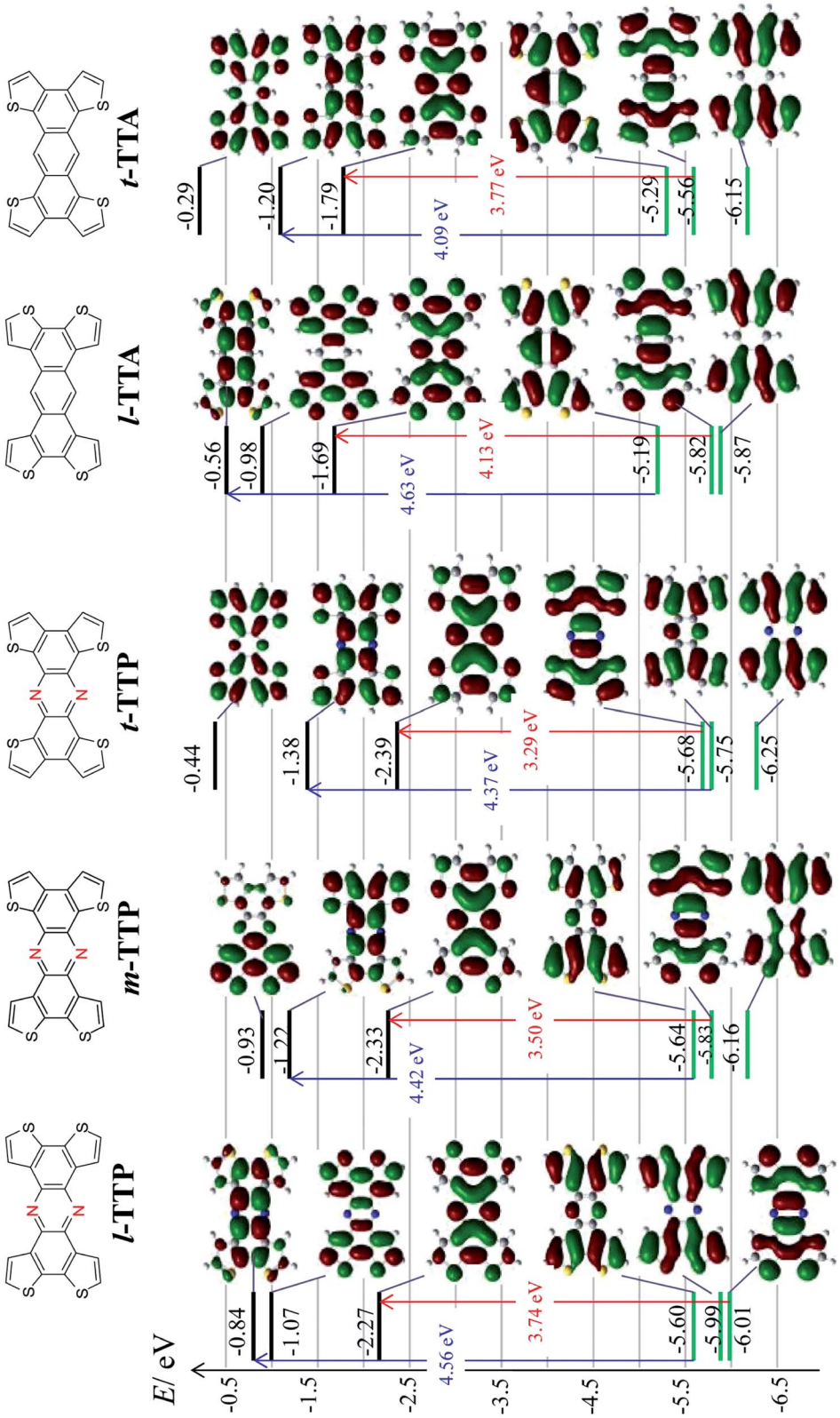

Fig. 10 Energies and spatial distributions of frontier orbitals of ***l*-TTP**, ***m*-TTP**, ***t*-TTP**, ***l*-TTA**, and ***t*-TTA**. Characteristic transitions are also indicated.

parameters and the evaluated intermolecular carrier mobilities along the crystal axes are listed in Table 5. In each case, hole mobilities of 0.5–5.0 $\times$ 10^{-1} cm^2 V^{-1} s^{-1} were predicted along π-staking directions and 10^{-3} to 10^{-2} cm^2 V^{-1} s^{-1} in the other directions. This result suggests that these crystals have reasonable potential for organic transistors.

Table 5 Calculated hopping mobilities of thiophene-fused phenazines

Molecules	Contact[a]	H_{ab}[b]/meV	S_{ab}[b]/meV	d/Å	V_{ab}/meV	λ[c]/meV	$\mu_{hopping}$/cm^2 V^{-1} s^{-1}
***l*-TTP**	a	7.7	−0.7	8.748	3.6	153	6.1×10^{-3}
***l*-TTP**	c'	14.5	−1.6	13.002	5.9	153	3.5×10^{-2}
***l*-TTP**	$(a + c)'$	3.2	−0.3	13.507	1.6	153	2.9×10^{-3}
***l*-TTP**	b'	−162.4	13.9	3.892	−91.3	153	7.6×10^{-1}
***m*-TTP**	a	−0.7	0.1	12.581	−0.3	169	8.9×10^{-5}
***m*-TTP**	b	−133.3	12.9	4.825	−66.5	169	5.0×10^{-1}
***m*-TTP**	$c_{//}'$	−1.8	−0.02	7.857	−1.9	169	1.1×10^{-3}
***m*-TTP**	$c_{\perp}$	25.9	−2.6	11.941	11.7	169	9.5×10^{-2}
***t*-TTP**	$b - a$	0.6	−0.2	12.314	−0.4	174	1.3×10^{-4}
***t*-TTP**	b	59.1	−7.4	5.014	20.2	174	4.7×10^{-2}
***t*-TTP**	$(a + c)'$	−24.1	2.4	9.262	−9.3	174	5.0×10^{-2}
***t*-TTP**	$a - c$	−8.3	0.9	11.862	−3.6	174	8.4×10^{-3}
***l*-HTTP**	t_1	−50.8	5.6	4.892	−25.0	155	8.7×10^{-2}
***l*-HTTP**	t_2	−3.9	0.4	12.749	−2.0	155	3.8×10^{-3}

[a] Corresponding molecular contacts are indicated in Fig. S17–S20. [b] Calculated at the PW91/TZ2P level. [c] Calculated at the B3LYP/6-31G(d) level.

Discussion

Synthesis

In the present work, a series of thiophene-fused phenazines have been synthesized in reasonable yields by a simple condensation reaction using only two types of diketones (**1a**, **1b**, **2a** and **2b**) as starting materials. Furthermore, both symmetric and asymmetric molecules can be prepared by this method, while the corresponding anthracene analogues require different synthetic routes for each molecule.[8] Recently, Reynolds *et al.*[15] also reported the synthesis of tetrathieno[3,2-*a*:2′,3′-*c*:3″,2″-*h*:2‴,3‴-*j*]phenazine (***l*-TTP**) by a condensation reaction between a diketone and a diamine. This method could be utilized widely for constructing fused polyaromatic compounds.

Effects of sulfur positions, introduction of nitrogen in the central ring, and substitution of alkyl chains on the electrochemical and optical properties of tetrathienophenazine derivatives

The estimated HOMO levels of the tetrathienophenazines from electrochemical experiments and DFT calculations were lower than those of the corresponding anthracene derivatives. This seems reasonable considering the introduction of an electron deficient aromatic ring. In the case of ***l*-TTP**, the frontier orbitals were estimated to be −5.60 and −2.27 eV for the HOMO and LUMO (Fig. 10), respectively, and those of the corresponding anthracene analogue (***l*-TTA**) were −5.19 and −1.69 eV (Fig. 10). On the other hand, the introduction of alkyl chains at the alpha positions of the fused thiophene rings increased the donor abilities. The effect of alkyl-substitution in these molecules was mainly seen in HOMO levels: the energy difference (increase) upon alkyl-substitution in the HOMO levels were 0.41, 0.43, and 0.36 eV for ***l*-TTP**, ***m*-TTP** and ***t*-TTP**, respectively, and these values were larger than the change in LUMOs (0.23, 0.41, and 0.28, respectively). This leads to bathochromic shifts in the absorption and fluorescence spectra upon both nitrogen introduction and alkyl-substitution of the molecules.

The absorption spectra of the phenazine derivatives showed two strong absorption bands, while those of the anthracene analogues showed only one strong absorption band, corresponding to the shorter wavelength band of the phenazine derivatives. This result was well reproduced by theoretical calculation: two absorption bands for all of the phenazine derivatives, and only one absorption band for the anthracene derivatives were predicted by TD-DFT calculations (Fig. S6–S13†). Although the orbital symmetries around the frontier orbitals (HOMO and LUMO) are not the same for each molecule, the symmetries of the molecular orbitals that contribute to the major two absorption bands are the same for all derivatives (Fig. S6–S11†). Furthermore, the two absorption bands consist of the same transitions, as summarized in Table S1.† For example, the two absorption bands in ***l*-TTP** are represented by a linear combination of two kinds of elemental transitions. One is the HOMO to LUMO+2 transition (4.56 eV) and the other is the HOMO−2 to LUMO transition (3.74 eV). These transition moments couple with each other to afford the two absorption bands (shorter and longer). Although the origin and the transition moments of the corresponding elemental transition in ***l*-TTA** are almost the same as that of ***l*-TTP**, the balance of the contributions of two transition moments for each band are not the same. This could be attributed to the energy difference in the frontier orbitals. Among the four molecular orbitals of ***l*-TTP** participating in these optical transitions, the HOMO and LUMO have significant coefficients at the nitrogen atoms in the central ring, while HOMO−2 and LUMO+2 do not have any coefficient because these are the nodal positions of the MOs. Compared with the energy difference from the corresponding MOs of ***l*-TTA**, the HOMO and LUMO of ***l*-TTP** are much lower than that of the HOMO−2 and LUMO+2. Since the nitrogen atoms with a larger electron negativity are introduced at the central ring, the energies of HOMO and LUMO are decreased to a large extent, while the effect on the other two orbitals was not as large, due to the nodal positions. In the case of ***l*-TTA**, the two transitions were assigned to HOMO to LUMO+2 (4.63 eV) and HOMO−1 to LUMO (4.13 eV), respectively. Since the transition energies are

close to each other, the transition moments couple effectively to cancel a longer absorption band, while the shorter absorption band is enhanced. On the other hand, the two transition moments in ***l*-TTP** have a relatively large difference so that the longer absorption band appears due to the imperfect cancellation between them.

The positions of the sulfur atoms also yield a significant difference in the orbital energies and absorption spectra. Both the HOMO and LUMO energies decrease in the order of ***l*-TTP** > ***m*-TTP** > ***t*-TTP** due to the effect of the different positions of the sulfur atoms (Fig. 10). The longer absorption bands showed obvious red shifts in the order of ***l*-TTP** > ***m*-TTP** > ***t*-TTP**. This feature was also preserved in the alkyl substituted molecules (Fig. 2). Since the longer absorption band is mainly due to transitions related to LUMO, the decrease in the LUMO energy mainly contributes to the red shift of the longer wavelength absorption bands in the order of ***l*-TTP** > ***m*-TTP** > ***t*-TTP** (Fig. 10). The position of the sulfur atoms in ***t*-TTP** results in the higher energy of the HOMO (−5.68 eV) contributing to the longer wavelength absorption in comparison with that of ***l*-TTP** (−6.01 eV).

The maximum emission wavelengths of ***l*-TTP**, ***m*-TTP** and ***t*-TTP** are nearly the same (Fig. 3) as each other in the fluorescence spectra, probably because the symmetry and orbital distribution of the excited molecular orbitals contributing to the emission are nearly the same, as shown in Fig. S14–S16.†

Crystal structures

The crystals of the three isomers, ***l*-TTP**, ***m*-TTP** and ***t*-TTP**, showed different packing structures. The different sulfur positions of these molecules lead to a difference in their molecular shape, intermolecular S···S contacts, distributions and energies of the molecular orbitals, and the resultant charge distributions. Since all these factors can contribute to the intermolecular packing structures, it is hard to conclude which is the most important factor to control the crystal structure in this case.

On the other hand, the difference in **TTP**s and **TTA**s is simpler. The replacement of the –CH= moieties of the **TTA**s with –N= does not change the molecular shape, and has little effect on the intermolecular S···S contacts although the molecular orbitals and the charge distributions should be affected. Actually, there are clear differences in the energies of the frontier orbitals and the charge distribution on the central ring between these systems. Furthermore, the characters of the HOMOs are different between ***t*-TTP** and ***t*-TTA**. Among the obtained crystals, ***l*-TTP** has the most different crystal structure from ***l*-TTA**, while ***t*-TTP** afforded an isostructural crystal with ***t*-TTA**. While the charge distributions on the central ring can mainly contribute to the π-stacking structure in this case, the S···S contacts are considered to affect both the π-stacking and the side-by-side interactions. The above result could be explained by means of the balance of the effects of charge distributions and the S···S contacts.

Transport properties

The experimental results of the field effect mobilities of thin films of these molecules were much lower than those of the theoretical predictions. This could be attributed to the different packing structures of the thin films from the crystals. The other factors for decreasing the charge mobility could be the relatively low HOMO energy and relatively large reorganization energy for the hole transfer process. These factors relate to the charge injection at the electrode semiconductor interface, and the charge transport processes in the bulk material, respectively.

The alkyl-substituted phenazines (***l*-HTTP**, ***m*-HTTP** and ***t*-HTTP**) showed nearly the same field effect transistor characteristics, probably because the thin films of these materials showed nearly the same crystallinity, although the positions of the sulfur atoms are different in these molecules. In comparison with the anthracene analogues, the alkyl-substituted phenazines showed lower FET mobilities ($\sim 10^{-6}$ cm^2 V^{-1} s^{-1}, compared with $\sim 10^{-2}$ cm^2 V^{-1} s^{-1} for the anthracene analogues). This could be due to the relatively low donor abilities and the large reorganization energies of the phenazines in comparison with the corresponding anthracenes, as discussed above.

Conclusion

In conclusion, we have synthesized a series of novel tetrathienophenazines by a simple condensation reaction between diketones and diamines. These materials were characterized by exact EI-MS, elemental analysis, NMR and single crystal X-ray crystallography. The hexylated derivatives showed much higher solubility than the unsubstituted derivatives in non-polar organic solvents. We studied the optical and electronic properties of these materials and found pronounced differences from their anthracene analogues. These materials showed two strong absorption bands, while the anthracene analogues only showed one strong absorption band in the UV-vis spectra. They also showed different fluorescence properties. The three unsubstituted derivatives (***t*-TTP**, ***m*-TTP** and ***l*-TTP**) showed light-blue fluorescence in chloroform, while ***t*-HTTP** showed green fluorescence and both ***m*-HTTP** and ***l*-HTTP** showed yellow fluorescence. The cyclic voltammograms indicated that the alkyl-substituted derivatives are weaker donors than their corresponding anthracene analogues. Thin films of these materials were prepared by sublimation, and different molecular packing structures and grains sizes were obtained when depositing at room temperature and at $T_{sub} = 75$ °C. Thin films of the alkyl-substituted derivatives show maximum field effect mobilities of $\sim 10^{-6}$ cm^2 V^{-1} s^{-1} when deposited at $T_{sub} =$ 75 °C, which was significantly larger than those formed at room temperature, due to a mono-oriented phase structure and bigger grains in the thin films. The conductivity of these materials can be improved by several orders of magnitude by iodine doping in the thin-film state and crystal state. The crystals and the thin films showed conductivities of 10^{-2} to 10^{-1} Ω^{-1} cm^{-1} and 10^{-7} to 10^{-5} Ω^{-1} cm^{-1} after chemical doping, respectively. We can conclude that these derivatives can also be utilized for organic electronics.

Experimental section

General procedures

All chemicals and solvents purchased were used without further purification, unless otherwise stated. Compound **1a**,[11] **2a**,[11] **8**[8]

and **10**[8] were synthesized according to reported procedures. NMR spectra were measured using a 400 MHz or 600 MHz JEOL WinAlpha A-600 using TMS as the internal reference. Low resolution and high resolution EI-MS spectra were measured using a JOEL JMS-T100GCV with perfluorokerosene (PFK) as the matrix. Cyclic voltammetry (CV) was carried out using a HOKUTO DENKO HZ-5000 under nitrogen gas. UV-vis spectra were measured using a JASCO V-570. Fluorescence spectra were measured using a JASCO FP-6600 and absolute fluorescence quantum yields were determined using a Hamamatsu C9920-02 calibrated integrating sphere system.

Preparation of 1b

n-Butyllithium (48 mL, 1.6 M in hexane, 76.8 mmol) was added dropwise to a solution of compound **11** (10.6 g, 31.6 mmol) in THF (150 mL) at −78 °C under N_2 gas. The mixture was stirred at −78 °C for 1 hour and diethyl oxalate (6.2 g, 42 mmol) was added to the mixture *via* a syringe at −78 °C. The mixture was stirred at −78 °C for 2 hours and then the temperature was allowed to slowly rise to room temperature. After stirring overnight, the obtained dark red mixture was quenched with saturated aqueous NH_4Cl, extracted by ethyl ether (200 mL × 3), and the combined organic layers were dried over Na_2SO_4. After removing the solvent, the residue was recrystallized from methanol–ethyl acetate (2/1) at −20 °C to yield a red solid (5.24 g, yield: 43%). IR ν_{max} = 3076 (w), 2924 (s), 2850 (s), 1645 (s), 1450 (m), 1404 (s), 1298 (m), 860 (w) cm^{-1}. High resolution EI-MS (M^+) for $C_{22}H_{28}O_2S_2$ found: 388.15234; calcd: 388.1531. ^1H NMR ($CDCl_3$, 400 MHz): δ 6.91 (2H, s), 2.88–2.84 (4H, t, J = 7.58 Hz), 1.76–1.68 (4H, m), 1.41–1.29 (12H, m), 0.92–0.88 (6H, t, J = 7.08 Hz); ^{13}C NMR ($CDCl_3$, 100 MHz): δ 173.56, 161.27, 143.00, 122.44, 122.29, 31.42, 31.06, 31.01, 28.64, 22.49, 14.10.

Preparation of 2b

n-Butyllithium (67 mL, 1.6 M in hexane, 101 mmol) was added dropwise to a mixture solution of compound **9** (22.95 g, 46.6 mmol) in anhydrous THF (150 mL) at −78 °C under N_2 gas. The mixture was stirred at −78 °C for 1 hour and diethyl oxalate (9.64 g, 66 mmol) was added to the mixture *via* a syringe at −78 °C. The mixture was stirred at −78 °C for 2 hours and then the temperature was allowed to slowly rise to 0 °C. The obtained dark blue mixture was quenched with saturated aqueous NH_4Cl, extracted with ethyl ether (300 mL × 3) and the combined organic layers were dried over Na_2SO_4. After removing the solvent, the residue was purified by chromatography, eluting with hexane–ethyl acetate (20 : 1, 10 : 1) to afford 8.06 g of a black solid (yield: 44%). IR ν_{max} = 2925 (s), 2857 (m), 1653 (s), 1397 (m), 845 (w) cm^{-1}. High resolution EI-MS (M^+) for $C_{22}H_{28}O_2S_2$ found: 388.1527; calcd: 388.1531. ^1H NMR ($CDCl_3$, 400 MHz): δ 7.12 (2H, s), 2.78–2.74 (4H, t, J = 7.40 Hz), 1.69–1.62 (4H, m), 1.38–1.31 (12H, m), 0.91–0.88 (6H, t, J = 6.80 Hz); ^{13}C NMR ($CDCl_3$, 100 MHz): δ 174.67, 146.51, 142.63, 134.59, 124.0 (×2), 31.42, 30.94, 29.84, 28.57 (×2), 22.54 (×2), 14.09 (×2).

Preparation of 3a

Benzo[1,2-*b*:4,3-*b*′]dithiophene-7,8-quinone (0.55 g, 2.5 mmol) and hydroxylamine hydrochloride (1.75 g, 25.0 mmol) in pyridine (3.0 mL) and ethanol (12.0 mL) were refluxed overnight. The reaction mixture was evaporated and the obtained light yellow residue was suspended in 20 mL of water, followed by dropwise addition of concentrated hydrochloric acid until pH ≤ 4. The mixture was filtered, washed with water and the filter cake was dried in a desiccator to afford a red solid (0.61 g, 97%). IR ν_{max} = 3166 (s), 3105 (s), 1653 (w), 1381 (m), 1125 (w) cm^{-1}. High resolution EI-MS (M^+) for $C_{10}H_6N_2O_2S_2$ found: 249.9865; calcd: 249.9871. ^1H NMR (acetone-d_6, 400 MHz): δ 7.97–7.96 (0.4H, d, J = 5.20 Hz), 7.81–7.80 (1H, d, J = 4.80 Hz), 7.67–7.66 (0.4H, d, J = 5.20 Hz), 7.60–7.59 (2H, d, J = 5.60 Hz); ^{13}C NMR (DMSO-d_6, 100 MHz): δ 143.25, 134.92, 131.78, 123.48, 122.70.

Preparation of 3b

Compound **1b** (0.388 g, 1.0 mmol) and hydroxylamine hydrochloride (0.7 g, 10.0 mmol) in pyridine (3.0 mL) and ethanol (15.0 mL) were stirred at 70 °C for 3 hours. The reaction mixture was evaporated and the obtained light yellow residue was suspended in 40 mL water–methanol = 2/1, followed by dropwise addition of concentrated hydrochloric acid until pH ≤ 4. The mixture was filtered, washed with water and the filter cake was dried in a desiccator to afford a red solid (0.39 g, 93%). IR ν_{max} = 3151 (m), 3045 (m), 2924 (s), 2857 (s), 1397 (m), 1275 (m), 821 (m) cm^{-1}. High resolution EI-MS (M^+) for $C_{22}H_{30}N_2O_2S_2$ found: 418.1756; calcd: 418.1749. ^1H NMR ($CDCl_3$, 400 MHz): δ 6.94 (2H, s), 2.85–2.81 (4H, t, J = 7.58 Hz), 1.74–1.70 (4H, m), 1.38–1.31 (12H, m), 0.91–0.88 (6H, t, J = 6.60 Hz); ^{13}C NMR ($CDCl_3$, 100 MHz): δ 153.6, 138.3, 137.0, 120.7, 120.0, 31.6, 31.3, 30.3, 28.9, 22.6, 14.1.

Preparation of 4a

A solution of $SnCl_2$ (anhydrous, 1.9 g, 10.0 mmol) in concentrated hydrochloric acid (5 mL) was added to a mixture of compound **3a** (0.5 g, 2.0 mmol) in ethanol (10 mL) at 0 °C. After stirring for 10 min, the mixture was taken to reflux for 3 h. The reaction mixture was filtered and washed with water and ethanol. The filter cake was suspended in saturated aqueous $NaHCO_3$ (30 mL) and extracted with CH_2Cl_2 (30 mL × 3). The organic phases were combined and dried over Na_2SO_4. Evaporation of the solvent afforded a beige powder (0.296 g, 67%). IR ν_{max} = 3394 (m), 3325 (m), 3272 (m), 3091 (w), 1486 (s), 1443 (s), 701 (s) cm^{-1}. High resolution EI-MS (M^+) for $C_{10}H_8N_2S_2$ found: 220.0136; calcd: 220.0129. ^1H NMR ($CDCl_3$, 600 MHz): δ 7.64–7.63 (2H, d, J = 5.16 Hz), 7.35–7.34 (4H, 2H, d, J = 4.38 Hz), 3.66 (br, s); ^{13}C NMR ($CDCl_3$, 150 MHz): δ 130.14, 129.05, 124.74, 122.94, 122.37.

Preparation of 4b

A solution of $SnCl_2$ (anhydrous, 0.90 g, 4.7 mmol) in concentrated hydrochloric acid (3 mL) was added to a mixture of compound **3b** (0.387 g, 0.9 mmol) in ethanol (20 mL) at 0 °C. The yellow solution became black immediately, and then it was

stirred at room temperature overnight. The reaction mixture was filtered and washed with water and ethanol. The filter cake was suspended in saturated aqueous $NaHCO_3$ (30 mL) and extracted with CH_2Cl_2 (30 mL × 3). The organic phases were combined and dried over Na_2SO_4. Evaporation of the solvent afforded a dark yellow solid (0.287 g, 80%). IR ν_{max} = 3409 (w), 3325 (w), 2924 (s), 2850 (m), 1616 (w), 1465 (m), 845 (w) cm^{-1}. High resolution EI-MS (M^+) for $C_{22}H_{32}N_2S_2$ found: 388.2006; calcd: 388.2007. ^1H NMR ($CDCl_3$, 400 MHz): δ 7.19 (2H, s), 3.46 (4H, s, br), 2.92–2.88 (4H, t, J = 7.08 Hz), 1.78–1.71 (4H, m), 1.40–1.30 (12H, m), 0.91–0.87 (6H, t, J = 7.08 Hz); ^{13}C NMR ($CDCl_3$, 100 MHz): δ 142.84, 128.63, 128.45, 124.00, 119.49, 31.61, 31.35, 30.87, 28.77, 22.56, 14.19.

Preparation of 5a

The preparation procedure was similar to that of compound **3a**. Yellow solid (yield: 99%). IR ν_{max} = 3228 (s), 3182 (s), 3113 (s), 2924 (m), 1600 (m), 1291 (m), 1125 (s) cm^{-1}. High resolution EI-MS (M^+) for $C_{10}H_6N_2O_2S_2$ found: 249.9867; calcd: 249.9871. ^1H NMR (DMSO-d_6, 400 MHz): δ 14.72 (0.4H, s), 12.36 (0.7H, s), 8.19–8.17 (0.7H, d, J = 5.36 Hz), 8.02–8.01 (0.8H, d, J = 5.36 Hz), 7.60–7.59 (0.7H, d, J = 5.36 Hz), 7.59–7.57 (0.5H, d, J = 5.36 Hz), 7.53–7.52 (0.8H, d, J = 5.36 Hz), 7.48–7.46 (0.5H, d, J = 5.36 Hz); ^{13}C NMR (DMSO-d_6, 150 MHz): δ 140.93, 134.82, 132.72, 130.56, 130.21, 127.38, 126.49, 125.44, 124.16, 124.03.

Preparation of 5b

The preparation procedure was similar to that of compound **3b**. Yellow solid (yield: 95%). IR ν_{max} = 2924 (s), 2857 (s), 2691 (br, m), 1132 (m), 1055 (m), 995 (m) cm^{-1}. High resolution EI-MS (M^+) for $C_{22}H_{30}N_2O_2S_2$ found: 418.1700; calcd: 418.1749. ^1H NMR (acetone-d_6, 600 MHz): δ 14.77 (0.5H, s), 11.94 (0.5H, s), 7.97 (1H, s), 7.22 (1H, s), 2.88–2.83 (4H, m), 1.73–1.68 (4H, m), 1.42–1.30 (12H, m), 0.90–0.88 (6H, m); ^{13}C NMR ($CDCl_3$, 100 MHz): δ 145.40, 145.13, 142.61, 141.20, 136.88, 130.73, 130.51, 127.38, 124.25, 120.72, 31.61, 31.57, 31.33, 31.11, 30.28, 30.19, 28.86, 28.80, 22.63, 22.57, 14.12, 13.97.

Preparation of 6a

The preparation procedure was similar to that of compound **4a**. Yellow solid (yield: 71%). High resolution EI-MS (M^+) for $C_{10}H_8N_2S_2$ found: 220.0133; calcd: 220.0129. ^1H NMR (DMSO-d_6, 600 MHz): δ 7.33–7.32 (2H, d, J = 5.46 Hz), 7.31–7.30 (2H, d, J = 5.10 Hz), 3.67 (4H, br, s); ^{13}C NMR (DMSO-d_6, 150 MHz): δ 126.22, 125.36, 124.98, 123.72, 120.28.

Preparation of 6b

The preparation procedure was similar to that of compound **4b**. Yellow-green solid (yield: 72%). IR ν_{max} = 2925 (s), 2857 (m), 1412 (w), 1313 (w), 836 (w) cm^{-1}. High resolution EI-MS (M^+) for $C_{22}H_{32}N_2S_2$ found: 388.2042; calcd: 388.2007. ^1H NMR ($CDCl_3$, 400 MHz): δ 6.92 (2H, s), 3.58 (4H, s, br), 2.90–2.86 (4H, t, J = 7.60 Hz), 1.77–1.70 (4H, m), 1.41–1.23 (12H, m), 0.90–0.87 (6H, t, J = 6.40 Hz); ^{13}C NMR ($CDCl_3$, 150 MHz): δ 143.94, 129.59, 124.77, 124.51, 116.74, 31.58, 31.28, 30.86, 28.76, 22.55, 14.07.

Preparation of 9 (ref. 16)

n-Butyllithium (72.4 mL, 1.6 M in hexane, 115.8 mmol) was added dropwise to the mixture of diisopropylamine (19.8 mL, 139 mmol) in anhydrous THF (80 mL) at −78 °C under N_2 gas. The mixture was stirred at −78 °C for 30 min and then the temperature was allowed to rise slowly to room temperature for 30 min. This freshly prepared LDA was added dropwise to the mixture of compound **8** (26.0 g, 105.2 mmol) in anhydrous THF (100 mL) at −78 °C under N_2 gas. The mixture was stirred at −78 °C for 1 hour and a red solution was observed. The temperature was allowed to rise slowly to −50 °C, and then $CuCl_2$ (15.6 g, 116 mmol) powder was added to the reaction, and the mixture was stirred overnight at −50 °C to RT. The dark green mixture was quenched with saturated aqueous NH_4Cl and a suspension was obtained. Aqueous HCl (20%) was added to the mixture until dissolution. The solution was extracted with ethyl ether (300 mL × 3) and the combined organic layers were dried over Na_2SO_4. After removing the solvent, the residue was recrystallized from methanol–ethyl acetate (2/1) at −20 °C. 22.08 g of a white crystalline solid was obtained (yield: 84%). High resolution EI-MS (M^+) for $C_{20}H_{28}Br_2S_2$ found: 490.0007; calcd: 489.9999. ^1H NMR ($CDCl_3$, 400 MHz): δ 6.71 (2H, s), 2.76–2.72 (4H, t, J = 7.80 Hz), 1.69–1.62 (4H, m), 1.40–1.28 (12H, m), 0.89–0.87 (6H, t, J = 5.84 Hz); ^{13}C NMR ($CDCl_3$, 100 MHz): δ 147.26, 127.54, 127.37, 110.84, 31.45, 30.97, 30.13, 28.69, 22.49, 14.09.

Preparation of 11 (ref. 16)

n-Butyllithium (84 mL, 1.6 M in hexane, 134 mmol) was added dropwise to a solution of compound **10** (26.0 g, 105.2 mmol) in anhydrous ethyl ether (200 mL) at −78 °C under N_2 gas. The mixture was stirred at −78 °C for 1 hour and then the temperature was allowed to rise slowly to −50 °C, and then $CuCl_2$ (18 g, 134 mmol) powder was added to the reaction, and the mixture was stirred overnight at −50 °C to RT. The dark green mixture was quenched with saturated aqueous NH_4Cl, and a suspension was obtained. Aqueous HCl (20%) was added to the mixture to dissolve the precipitate. The solution was extracted with ethyl ether (200 mL × 3) and the combined organic layers were dried over Na_2SO_4. After removing the solvent, the residue was recrystallized from methanol–ethyl acetate (2/1) at −20 °C. 10.64 g of a white solid was obtained (yield: 52%). IR ν_{max} = 2932 (s), 2857 (m), 1532 (w), 1457 (w), 792 (w) cm^{-1}. High resolution EI-MS (M^+) for $C_{20}H_{30}S_2$ found: 334.1788; calcd: 334.1789. ^1H NMR ($CDCl_3$, 400 MHz): δ 7.08 (2H, s), 6.97 (2H, s), 2.82–2.78 (4H, t, J = 7.56 Hz), 1.72–1.64 (4H, m), 1.41–1.29 (12H, m), 0.91–0.87 (6H, t, J = 7.08 Hz); ^{13}C NMR ($CDCl_3$, 100 MHz): δ 146.37, 137.11, 123.34 (×2), 116.91 (×2), 31.57, 30.13, 28.77, 22.56, 14.15, 13.99.

Preparation of *t*-TTP

Benzo[1,2-*b*:4,3-*b*′]dithiophene-7,8-quinone (0.29 g, 1.3 mmol) and compound **4a** (0.29 g, 1.3 mmol) in ethanol (10.0 mL) were refluxed for 16 h. The reaction mixture was cooled to RT, filtered and washed with ethanol. The filter cake was dried in the desiccator to afford an orange crude powder (0.42 g). The crude product was sublimed (280 °C) to obtain 310 mg of an orange

crystalline solid. The crystals were of suitable quality to be used for X-ray characterization. NMR data are not available due to poor solubility. IR ν_{max} = 3097 (m), 1532 (m), 1404 (s), 1344 (m), 1214 (m), 723 (m) cm^{-1}. High resolution EI-MS (M^+) for $C_{20}H_8N_2S_4$ found: 403.9565; calcd: 403.9570. Elemental analysis (%) for $C_{20}H_8N_2S_4$ found: C 59.24, H 2.03, N 6.68; calcd: C 59.38, H 1.99, N 6.92%.

Preparation of *l*-TTP

The preparation procedure was similar to compound ***t*-TTP**. Crystals suitable for X-ray characterization were obtained. Red solid (yield: 53%). NMR data are not available due to poor solubility. IR ν_{max} = 3111 (m), 1495 (m), 1411 (m), 1312 (m), 1214 (m), 723 (s) cm^{-1}. High resolution EI-MS (M^+) for $C_{20}H_8N_2S_4$ found: 403.9568; calcd: 403.9570. Elemental analysis (%) for $C_{20}H_8N_2S_4$ found: C 59.30, H 1.88, N 6.51; calcd: C 59.38, H 1.99, N 6.92%.

Preparation of *m*-TTP

The preparation procedure was similar to that of compound ***t*-TTP**. Yellow solid (yield: 41%). NMR data were not available due to poor solubility. IR ν_{max} = 3090 (m), 1510 (m), 1404 (s), 1312 (s), 723 (s) cm^{-1}. High resolution EI-MS (M^+) for $C_{20}H_8N_2S_4$ found: 403.9567; calcd: 403.9570. Elemental analysis (%) for $C_{20}H_8N_2S_4$ found: C 59.38, H 1.81, N 6.54; calcd: C 59.38, H 1.99, N 6.92%.

Preparation of *t*-HTTP

Compound **3b** (0.160 g, 0.41 mmol) and compound **4b** (0.165 g, 0.42 mmol) in ethanol (20.0 mL) were refluxed for 48 h. The reaction mixture was cooled to RT, filtered and washed with methanol (10.0 mL). The filter cake was dried in the desiccator to afford a yellow solid (0.12 g, 40%). IR ν_{max} = 2924 (s), 2857 (m), 1412 (m), 966 (w), 814 (w) cm^{-1}. High resolution EI-MS (M^+) for $C_{44}H_{56}N_2S_4$ found: 740.3322; calcd: 740.3326. ^{1}H NMR ($CDCl_3$, 600 MHz): δ 7.36 (4H, s), 3.06–3.03 (8H, t, J = 7.53 Hz), 1.88–1.84 (8H, m), 1.47–1.35 (24H, m), 0.92–0.90 (12H, t, J = 6.78 Hz); ^{13}C NMR ($CDCl_3$, 150 MHz): δ 150.96, 136.87, 135.94, 133.39, 119.93, 31.63, 31.54, 31.14, 28.85, 22.59, 14.10. Elemental analysis (%) for $C_{44}H_{56}N_2S_4$ found: C 70.73, H 7.49, N 3.56; calcd: C 71.30, H 7.62, N 3.78%.

Preparation of *l*-HTTP

The preparation procedure was similar to that of compound ***t*-HTTP**. Yellow solid (yield: 75%). IR ν_{max} = 2924 (s), 2857 (m), 1419 (w), 1223 (w), 836 (w) cm^{-1}. High resolution EI-MS (M^+) for $C_{44}H_{56}N_2S_4$ found: 740.3321; calcd: 740.3326. ^{1}H NMR ($CDCl_3$, 600 MHz): δ 8.17 (4H, s), 3.08–3.05 (8H, t, J = 7.68 Hz), 1.90–1.85 (8H, m), 1.54–1.34 (24H, m), 0.94–0.91 (12H, t, J = 7.14 Hz); ^{13}C NMR ($CDCl_3$, 150 MHz): δ 144.93, 137.10, 134.53, 134.86, 121.24, 31.65, 31.62, 30.82, 28.89, 22.60, 14.11. Elemental analysis (%) for $C_{44}H_{56}N_2S_4$ found: C 71.11, H 7.44, N 3.59; calcd: C 71.30, H 7.62, N 3.78%.

Preparation of *m*-HTTP

The preparation procedure was similar to that of compound ***t*-HTTP**. Yellow solid (yield: 56%). IR ν_{max} = 2924 (s), 2850 (m), 1518 (w), 1412 (w), 814 (w) cm^{-1}. High resolution EI-MS (M^+) for $C_{44}H_{56}N_2S_4$ found: 740.3325; calcd: 740.3326. ^{1}H NMR ($CDCl_3$, 400 MHz): δ 8.13 (2H, s), 7.42 (2H, s), 3.09–3.03 (8H, m), 1.90–1.84 (8H, m), 1.56–1.36 (24H, m), 0.93–0.90 (12H, m); ^{13}C NMR ($CDCl_3$, 100 MHz): δ 150.78, 144.87, 137.15, 136.81, 136.00, 134.25, 133.76, 133.67, 121.32, 120.02, 31.69, 31.64, 31.59, 31.16, 30.79, 28.90, 28.86, 22.67, 22.63, 22.60, 14.19, 14.04. Elemental analysis (%) for $C_{44}H_{56}N_2S_4$ found: C 71.19, H 7.52, N 3.61; calcd: C 71.30, H 7.62, N 3.78%.

Crystal growth and X-ray analysis

Crystals of ***t*-TTP** were obtained by slow evaporation of the DCM solution or sublimation at 280–290 °C, and the crystal parameters obtained by these two methods were the same. Crystals of ***m*-TTP** were grown by slow cooling of a saturated benzonitrile solution from 160–90 °C. Crystals of ***l*-TTP** were obtained by sublimation at 300–320 °C. Crystals of ***l*-HTTP** were grown by slowly evaporating a DCM solution. Crystals of ***m*-HTTP** and ***t*-HTTP** could not be obtained under various conditions. Crystals were mounted on a loop using oil (CryoLoop, Immersion Oil, Type B; Hampton Research Corp.) and set on a Rigaku RA-Micro007 with a Saturn CCD detector using graphite-monochromated Mo Kα radiation (λ = 0.710690 Å) under a cold nitrogen steam. The frame data were integrated and corrected for absorption with the Rikagu/MSC CrystalClear package.[17] The structures were solved by direct methods[18] and standard difference map techniques, and were refined with full-matrix least-squares procedures on F^2 by a Rikagu/MSC CrystalStructure package. Anisotropic refinement was applied to all non-hydrogen atoms. All hydrogen atoms were placed at calculated positions and refined using a riding model.

Theoretical calculations

The molecular orbital calculations based on density functional theory were carried out using the Gaussian09, revision C.01 program package.[13] The molecular structures were optimized using HF and B3LYP[19] methods with 6-31G(d) basis sets.

Intermolecular hopping carrier mobilities were calculated on the basis of Marcus theory.[14] First, intermolecular electronic coupling matrix elements (V_{ab}) were calculated with eqn (1) using intermolecular charge transfer integrals (H_{ab}), overlap integrals (S_{ab}), and the energies of the two molecular orbitals (H_{aa} and H_{bb}) calculated at the PW91/TZ2P level using the ADF 2012 program package.

$$V_{ab} = \frac{H_{ab} - S_{ab}(H_{aa} - H_{bb})/2}{1 - {S_{ab}}^2} \quad (1)$$

Then the intermolecular charge transfer rate constants (k_{ET}) were evaluated from eqn (2).

$$k_{ET} = \frac{{V_{ab}}^2}{h}\left(\frac{\pi}{\lambda k_B T}\right)^{1/2} \exp\left(-\frac{\lambda}{4k_B T}\right) \quad (2)$$

where h, k_B, and T are Planck's constant, Boltzmann constant, and temperature, respectively. The reorganization energies upon intermolecular hole transfer (λ) were obtained from $\lambda = (E^{+}* - E^{+}) + (E* - E)$, where E, E^{+}, $E*$, and $E^{+}*$ are the heat of formations for an optimized neutral molecule, optimized cation molecule, neutral state on cation structure, and cation state on neutral structure, respectively, calculated at the B3LYP/6-31G(d) level. Intermolecular hopping mobilities (μ) were estimated from the following eqn (3).

$$\mu_{\text{hopping}} = \frac{ed^2}{k_B T} k_{ET} \quad (3)$$

where d is the intermolecular center-to-center distance of adjacent molecules.

Thin-film X-ray analysis

X-ray diffractions of vapor deposited thin films on bare Si substrates were obtained using a Rikagu Smartlab X-ray diffractometer with a Cu Kα source (λ = 1.541 Å) in air. The calculated inter-layer distances (d-spacing) are listed in Table 3.

Fabrication of the thin-film transistors

Thin films were deposited on an interdigitated Pt electrode array with a gap of 2 μm over a 2 × 2 mm area (corresponding to 2 μm gap and 1 m width) as source/drain electrodes (bottom-contact) patterned on n-doped silicon substrates covered with a 300 nm thick SiO_2 layer. Prior to deposition, the substrates were cleaned by sonication in acetone and isopropyl alcohol, followed by exposure to O_2 plasma. Films were deposited by vacuum sublimation (pressure $\sim 5 \times 10^{-4}$ Pa) at a deposition rate 0.2–1.2 Å s^{-1} until a thickness of 100 nm was reached. Organic field-effect transistor measurements were carried out in a vacuum with a Keithley 2636A dual channel source meter. The field-effect mobility (μ_{FET}) was calculated in the linear region of transfer curves.

Conductivity measurements upon chemical doping

The electrical conductivity of the thin-films was measured by a dc two-probe method utilizing the substrates from FET measurements. The conductivity measurements on crystalline samples were carried out by connecting gold wires at the opposite edges of the crystal with gold paste. The sample was placed in a glass chamber with a nitrogen atmosphere and iodine vapor was gradually introduced into the chamber through a valve. In each case, 1 V of constant voltage was applied to the sample and the current was recorded with Keithley 487 picoammeter upon iodine doping.

Acknowledgements

The authors gratefully acknowledge financial support by a Grant-in-Aid for Scientific Research from the Ministry of Education, Culture, Sports, Science and Technology (MEXT) of Japan. The authors also thank Prof. Shigehiro Yamaguchi, Dr Aiko Fukuzawa and Mr Kazuhiko Nagura (Nagoya University) for their help in measuring the absolute quantum yield of the obtained materials.

Notes and references

1 (*a*) A. Heckmann and C. Lambert, *Angew. Chem., Int. Ed.*, 2012, **51**, 326–392; (*b*) G. Heimel, I. Salzmann, S. Duhm and N. Koch, *Chem. Mater.*, 2011, **23**, 359–377; (*c*) S. Lo and P. L. Burn, *Chem. Rev.*, 2007, **107**, 1097–1116; (*d*) Q. Zhang, J. Li, K. Shizu, S. Huang, S. Hirata, H. Miyazaki and C. Adachi, *J. Am. Chem. Soc.*, 2012, **134**, 14706–14709; (*e*) L. Deng, X. Wang, Z. Zhang and J. Li, *J. Mater. Chem.*, 2012, **22**, 19700–19708; (*f*) O. Usluer, S. Demic, D. Egbe, E. Tozlu, C. Birchner, A. Pivrikas, A. M. Ramil and N. S. Sariciftci, *Adv. Funct. Mater.*, 2010, **20**, 4152–4161; (*g*) B. Yan, C. C. C. Cheung, S. C. F. Kui, H. Xiang, V. A. L. Roy, S. Xu and C. Che, *Adv. Mater.*, 2007, **19**, 3599–3603; (*h*) Y. Yu, O. Solomeshch, H. Chechik, A. A. Goryunkov, R. F. Tuktarov, D. H. Choi, J. Jin, Y. Eichen and N. Tessler, *J. Appl. Phys.*, 2008, **104**, 124505.

2 (*a*) C. Li and H. Wonneberger, *Adv. Funct. Mater.*, 2012, **24**, 613–616; (*b*) C. Li, M. Liu, N. G. Pschirer, M. Baumgarten and K. Muellen, *Chem. Rev.*, 2010, **110**, 6817–6855; (*c*) X. Zhang and D. Zhu, *Polym. Chem.*, 2010, **1**, 409–419; (*d*) T. W. Holcombe, C. H. Woo, D. F. J. Kavulak, B. C. Thompson and J. M. J. Frechet, *J. Am. Chem. Soc.*, 2009, **131**, 14160–14161; (*e*) E. Lim, S. Lee and K. K. Lee, *Mol. Cryst. Liq. Cryst.*, 2012, **565**, 98–105; (*f*) F. Wuerthner and K. Meerholz, *Chem.–Eur. J.*, 2010, **16**, 9366–9373.

3 (*a*) A. Saeki, Y. Koizumi, T. Aida and S. Seki, *Acc. Chem. Rev.*, 2012, **45**, 1193–1203; (*b*) H. Usta, A. Facchetti and T. J. Marks, *Acc. Chem. Rev.*, 2011, **44**, 501–510; (*c*) M. Tang and Z. N. Bao, *Chem. Mater.*, 2011, **23**, 446–455; (*d*) A. L. Kanibolotsky, I. F. Perepichka and P. J. Skabara, *Chem. Soc. Rev.*, 2010, **39**, 2695–2728; (*e*) W. Wu, Y. Liu and D. Zhu, *Chem. Soc. Rev.*, 2010, **39**, 1489–1502; (*f*) H. Huang, Z. Chen, R. P. Ortiz, C. Newman, H. Usta, L. X. Chen, *et al.*, *J. Am. Chem. Soc.*, 2012, **134**, 10966–10973; (*g*) M. L. Tang, T. Okamoto and Z. Bao, *J. Am. Chem. Soc.*, 2006, **128**, 16002–16003; (*h*) K. Xiao, Y. Liu, W. Zhang, F. Wang, J. Gao, W. Qiu, Y. Ma, G. Cui, S. Chen, *et al.*, *J. Am. Chem. Soc.*, 2005, **127**, 13281–13286.

4 (*a*) K. Niimi, S. Shinamura, I. Osaka, E. Miyazaki and K. Takimiya, *J. Am. Chem. Soc.*, 2011, **133**, 8732–8739; (*b*) T. Yamamoto and K. Takimiya, *J. Am. Chem. Soc.*, 2007, **129**, 2224–2225; (*c*) M. Uno, Y. Tominari, M. Yamagishi, I. Doi, E. Miyazaki, K. Takimiya and J. Takeya, *Appl. Phys. Lett.*, 2009, **94**, 223–308; (*d*) M. J. Kang, I. Doi, H. Mori, E. Miyazaki, K. Takimiya, M. Ikeda and H. Kuwabara, *Adv. Mater.*, 2011, **23**, 1222–1225; (*e*) K. Nakayama, Y. Hirose, J. Soeda, M. Yoshizumi, T. Uemura, M. Uno, W. Li, M. J. Kang, M. Yamagishi, Y. Okada, E. Miyazaki, Y. Nakazawa, A. Nakao, K. Takimiya and J. Takeya, *Adv. Mater.*, 2011, **23**, 1626–1629.

5 K. Takimiya, Y. Kunugi, Y. Toyoshima and T. Otsubo, *J. Am. Chem. Soc.*, 2005, **127**, 3605–3612.

6 H. Ebata, T. Izawa, E. Miyazaki, K. Takimiya, M. Ikeda, H. Kuwabara and T. Yui, *J. Am. Chem. Soc.*, 2007, **129**, 15732–15733.

7 (*a*) H. Hussain, S. Specht, S. R. Sarite, M. Saeftel, A. Hoerauf, B. Schulz and K. Krohn, *J. Med. Chem. Soc.*, 2011, **54**, 4913–4917; (*b*) M. Putala, N. Kastner-Pustet and A. Mannschreck, *Tetrahedron: Asymmetry*, 2001, **12**, 3333–3342.

8 J. L. Brusso, O. D. Hirst, A. Dadvand, S. Ganesan, F. Cicoira, C. M. Robertson, R. T. Oakley, F. Rosei and D. F. Perepichka, *Chem. Mater.*, 2008, **20**, 2484–2494.

9 W. Liu, Y. Zhou, Y. Ma, Y. Cao, J. Wang and J. Pei, *Org. Lett.*, 2007, **9**, 4187–4190.

10 L. Carlier, M. Baron, A. Chamayou and B. Couarrze, *Tetrahedron Lett.*, 2011, **52**, 4686–4689.

11 A. Meyer, E. Sigmund, F. Luppertz, G. Schnakenburg, I. Gadaczek, T. Bredow, S. Jester and S. Höger, *Beilstein J. Org. Chem.*, 2010, **6**, 1180–1187.

12 B. W. D'Andrade, S. Datta, S. R. Forrest, P. Djurovich, E. Polikarpov and M. E. Thompson, *Org. Electron.*, 2005, **6**, 11–20.

13 M. J. Frisch, G. W. Trucks, H. B. Schlegel, G. E. Scuseria, M. A. Robb, J. R. Cheeseman, J. A. J. Montgomery, T. Vreven, K. N. Kudin, J. C. Burant, J. M. Millam, S. S. Iyengar, J. Tomasi, V. Barone, B. Mennucci, M. Cossi, G. Scalmani, N. Rega, G. A. Petersson, H. Nakatsuji, M. Hada, M. Ehara, K. Toyota, R. Fukuda, J. Hasegawa, M. Ishida, T. Nakajima, Y. Honda, O. Kitao, H. Nakai, M. Klene, X. Li, J. E. Knox, H. P. Hratchian, J. B. Cross, V. Bakken, C. Adamo, J. Jaramillo, R. Gomperts, R. E. Stratmann, O. Yazyev, A. J. Austin, R. Cammi, C. Pomelli, J. W. Ochterski, P. Y. Ayala, K. Morokuma, G. A. Voth, P. Salvador, J. J. Dannenberg, V. G. Zakrzewski, S. Dapprich, A. D. Daniels, M. C. Strain, O. Farkas, D. K. Malick, A. D. Rabuck, K. Raghavachari, J. B. Foresman, J. V. Ortiz, Q. Cui, A. G. Baboul, S. Clifford, J. Cioslowski, B. B. Stefanov, G. Liu, A. Liashenko, P. Piskorz, I. Komaromi, R. L. Martin, D. J. Fox, T. Keith, M. A. Al-Laham, C. Y. Peng, A. Nanayakkara, M. Challacombe, P. M. W. Gill, B. Johnson, W. Chen, M. W. Wong, C. Gonzalez and J. A. Pople, *Gaussian 03, Revision C.02*, Gaussian, Inc., Wallingford, CT, 2004.

14 (*a*) M. D. Newton, *Chem. Rev.*, 1991, **91**, 767–792; (*b*) K. Senthilkumar, F. C. Grozema, F. M. Bickelhaupt and L. D. A. Siebbeles, *J. Chem. Phys.*, 2003, **119**, 9809–9816; (*c*) K. Senthikumar, F. C. Grozem, C. Fonseca Guerra, F. M. Bickelhaupt, F. D. Lewis, Y. A. Berlin, M. A. Rantner and L. D. A. Siebbeles, *J. Am. Chem. Soc.*, 2005, **127**, 14894–14903.

15 F. A. Arroyave, C. A. Richard and J. R. Reynolds, *Org. Lett.*, 2012, **14**, 6138–6141.

16 (*a*) S. Marder and Y. A. Getmanenko, *US Pat.*, no. WO/2011/098495, 2011; (*b*) Y. A. Getmaneko, P. Tongwa, T. V. Timofeeva and S. R. Marder, *Org. Lett.*, 2010, **12**, 2136–2139.

17 (*a*) CrystalClear, Rigaku Corporation, 1999; CrystalClear Software User's Guide, Molecular Structure Corporation, 2000; J. W. Pflugrath, *Acta Crystallogr., Sect. D*, 1999, **55**, 1718–1725; (*b*) CrystalStructure 3.8: Crystal Structure Analysis Package, Rigaku and Rigaku Americas, 9009 New Trails Dr., The Woodlands, TX, USA, 2000–2007.

18 G. M. Sheldrick, *SHELX97*, 1997.

19 (*a*) A. D. Becke, *Phys. Rev. A: At., Mol., Opt. Phys.*, 1988, **38**, 3098; (*b*) A. D. Becke, *J. Chem. Phys.*, 1993, **98**, 5648; (*c*) C. Lee, W. Yang and R. G. Parr, *Phys. Rev. B: Condens. Matter Mater. Phys.*, 1988, **37**, 785; (*d*) P. J. Stephens, F. J. Devlin, C. F. Chabalowski and M. J. Frisch, *J. Phys. Chem.*, 1994, **98**, 11623.